Supplemental Material

Future benefits of emission controls in mitigating climate-driven regional transport of $PM_{2.5}$ in China

Shansi Wang[1,2], Siwei Li[1,2,3*], Jia Xing[4], Yu Ding[1,2], Senlin Hu[1,2], Shuchang Liu[4], Yu Qin[5], Zhaoxin Dong[4], Jiaxin Dong[1,2], Ge Song[1,2], Lechao Dong[6,7], Chunying Fan[1,2] , Mengfan Teng[1,2], Ge Han[2], Xin Ma[3], Jinjun Lu[8]

1 Hubei Key Laboratory of Quantitative Remote Sensing of Land and Atmosphere, Wuhan University, Wuhan 430079, China

2 School of Remote Sensing and Information Engineering, Wuhan University, Wuhan, 430079, China

3 State Key Laboratory of Information Engineering in Surveying, Mapping and Remote Sensing, Wuhan University, Wuhan, 430079, China

4 School of Environment, Tsinghua University, Beijing, 100084,China

5 Map Institute of Guangdong Province, Guangzhou, 510075, China

6 CMA Earth System Modeling and Prediction Centre (CEMC), China Meteorological Administration, Beijing 100081, China;

7 State Key Laboratory of Severe Weather, Chinese Academy of Meteorological Sciences, China Meteorological Administration, Beijing 100081, China

8 School of Physics and Electronic-information Engineering, Hubei Engineering University

Corresponding author:

Siwei Li (siwei.li@whu.edu.cn)

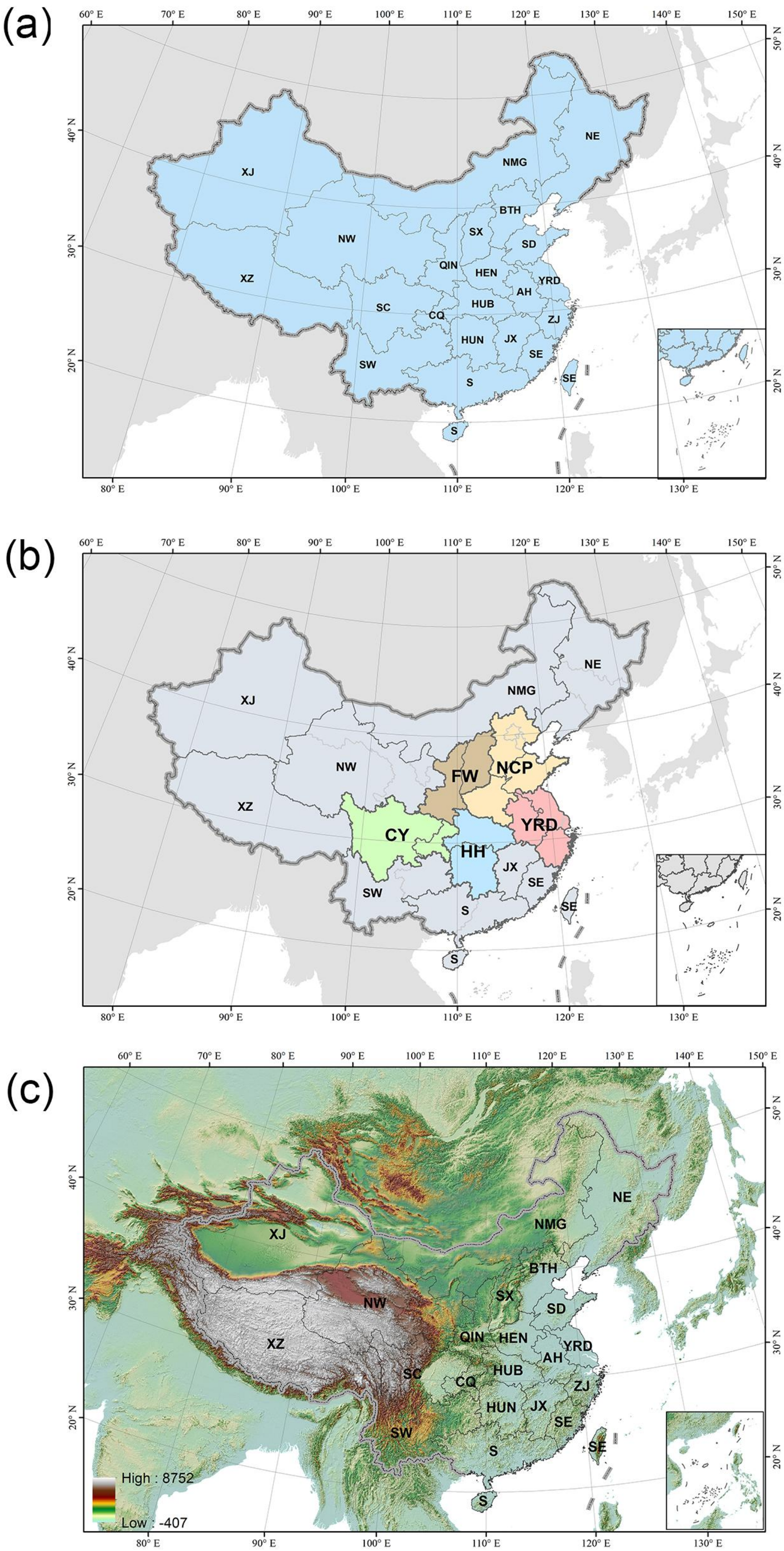
(a)
XJ
NE
NMG
BTH
SX
SD
NW
XZ
QIN
HEN
AH
YRD
SC
CQ
HUB
ZJ
HUN
JX
SE
SW
S
(b)
FW
NCP
YRD
CY
HH
(c)
High : 8752
Low : -407

Figure S1. The quasi-provinces administrative division and topography in China

(a) 21 tagged regions, including five principal regions, are differentiated by color.

21 tagged regions are Beijing, Tianjin city and Hebei Province noted as BTH. Jiangsu-Shanghai including Jiangsu Province and Shanghai city. Southeast (SE) including two Province (Fujian and Taiwai Province). South including three Province (Guangdong, Guangxi and Hainan Province, Hong Kong special administrative region). Southwest (WE) including two Province (Yunnan and Guizhou Province). Northwest (NW) including three province (Qinghai, Gansu, and Ningxia Province). Northeast (NE) including three Province (Heilongjiang, Jilin and Liaoning Province). Other provinces are tagged individually. Thus all 21 tagged regions are NE, Neimenggu (NMG), BTH, Shandong (SD), Shanxi (SX), Shaanxi (QIN), Henan (Henan), Hubei (HUB), Hunan (HUN), Jiangxi (JX), Anhui (AH), Jiangsu-Shanghai (JS) Zhejiang (ZJ), SE, S, SW, NW, Xizang (XZ), Xinjiang (XJ), Chongqing (CQ), Sichuan (SC), respectively.

(b) Five key regions discussed, including the North China Plain (denoted as NCP, including Beijing-Tianjin-Hebei region, Shandong and Henan province), the the Yangtze River Delta (denoted as YRD, including Jiangsu-Shanghai region, Zhejiang and Anhui province), the Central China (denoted as HH, including Hubei and Hunan province), Chengyu area (denoted as CY, including Sichuan province and Chongqing region) and the Feiwen Plain (denoted as FW, including Shanxi and Shaanxi province).

(c) The Digital Elevation Model (DEM) of China (unit: meters)

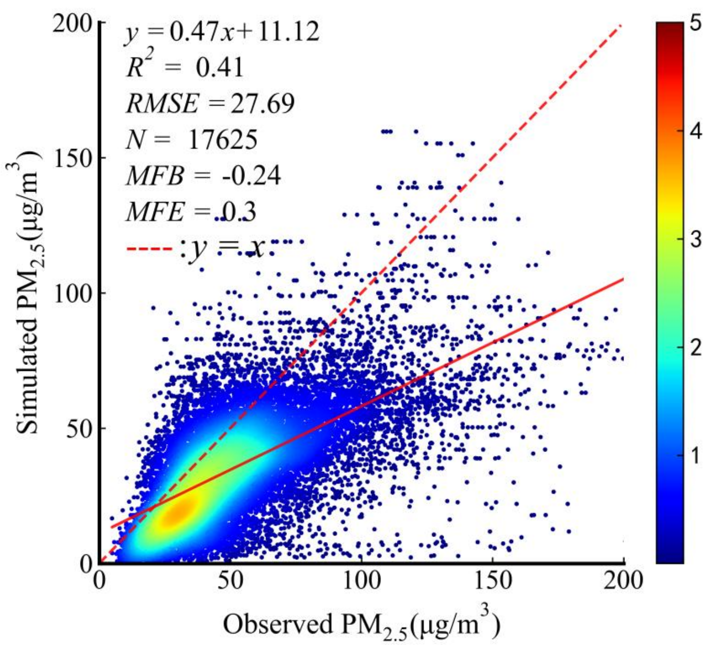

Figure S2. Model performance

RMSE: root mean square error ;

MFB: the mean fractional bias

MFE: mean fractional error

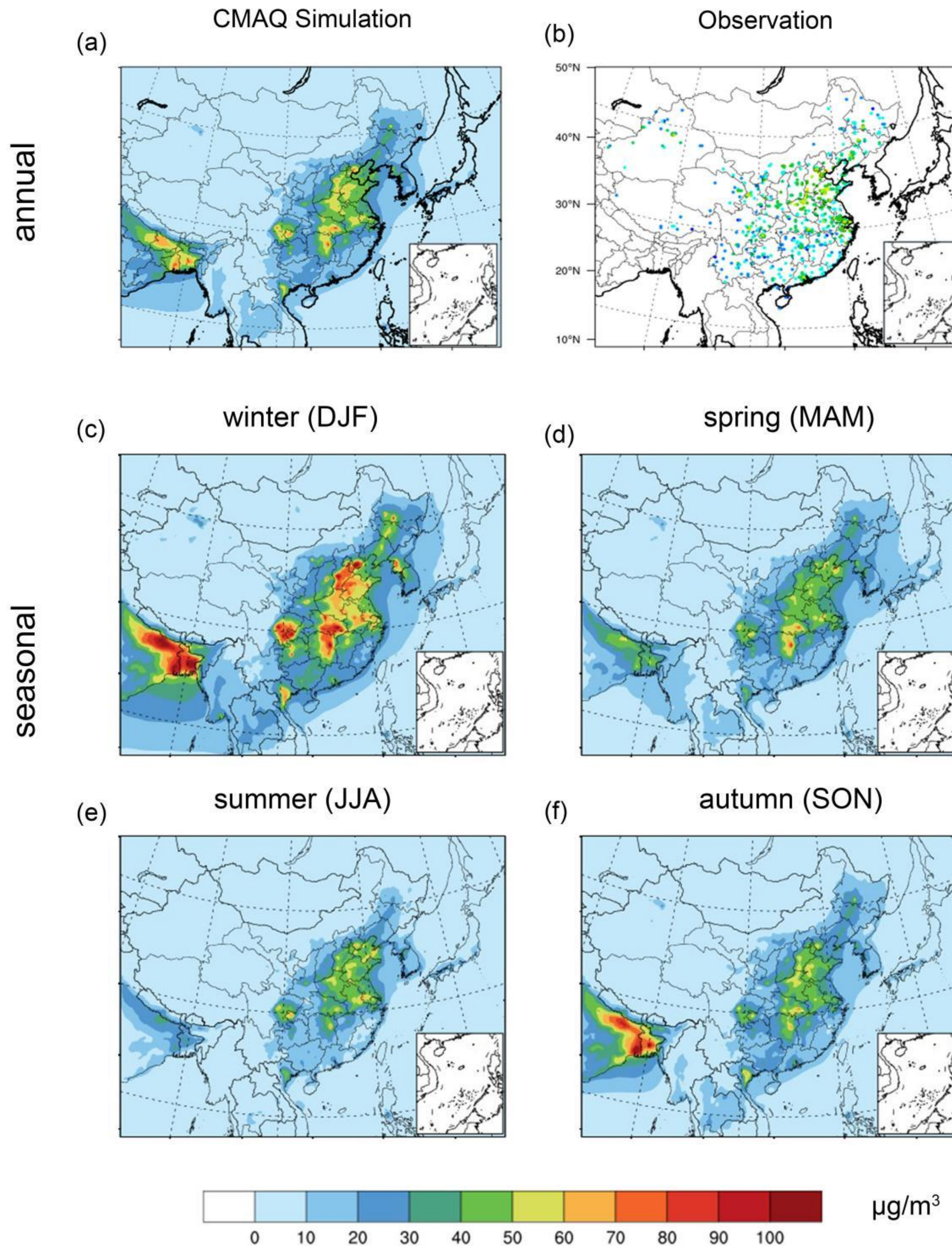

Figure S3. Annual and seasonal simulated and observed $PM_{2.5}$ concentration in 2015 REF baseline. (a) shows the annual CMAQ simulation, (b) shows the annual $PM_{2.5}$ observation of monitoring station, (c), (d), (e), (f) show winter (December, January, February, DJF), spring (March, April, May, MAM), summer (June, July, August, JJA), and autumn (September, October, November, SON), respectively.

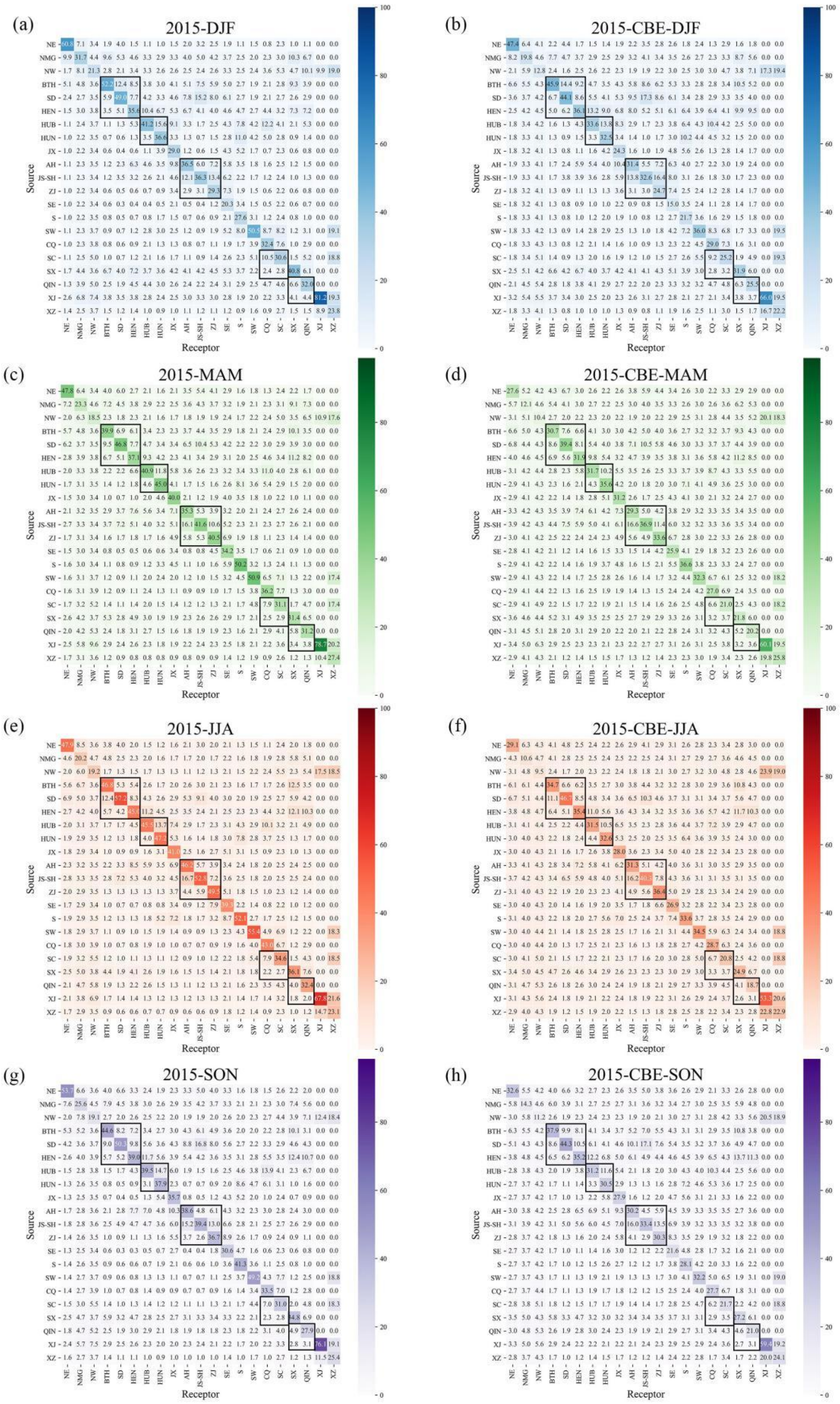

Figure S4. Seasonal transport matrix (percentage) for 12 month in 2015 baseline. The left and right panel show REF and CBE scenario, respectively. From top to bottom row represent winter (December, January, February, DJF), spring (March, April, May, MAM), summer(June, July, August, JJA), and autumn (September, October, November, SON), respectively.

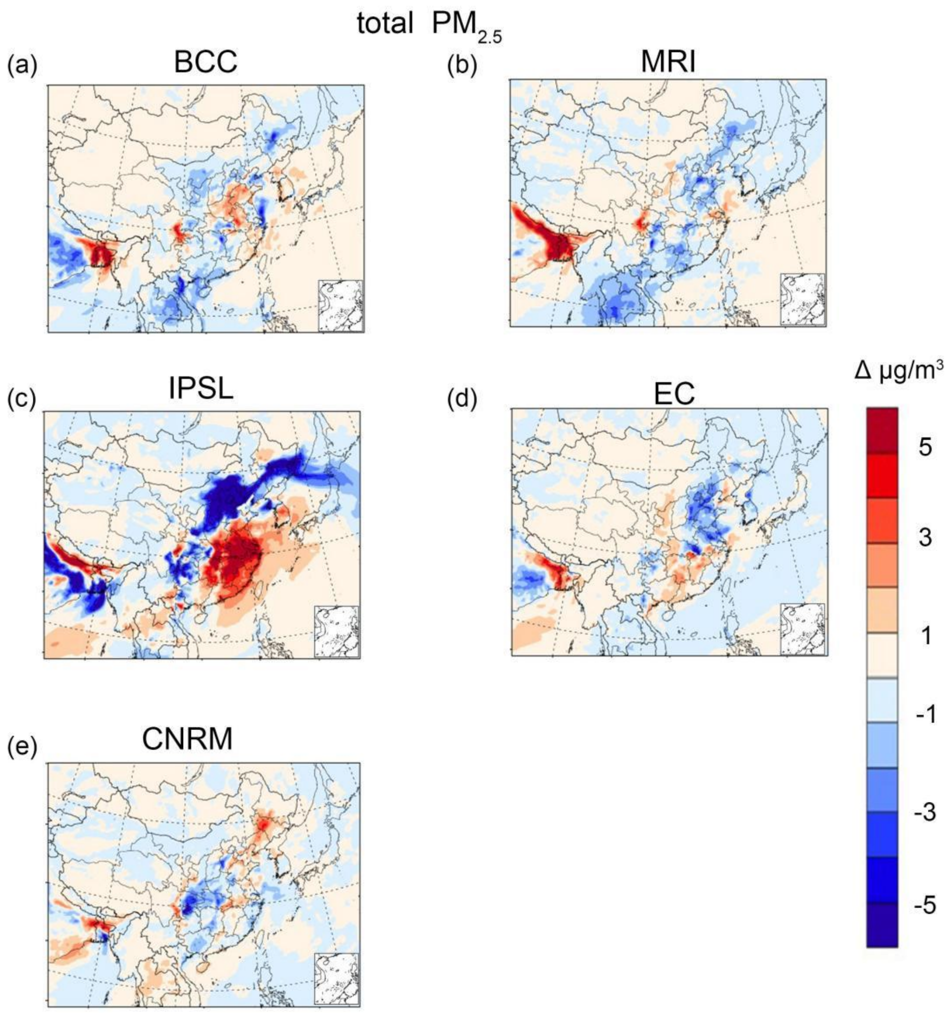

Figure S5. The distribution of annual average differences in simulated $PM_{2.5}$ total concentrations between the SSP126 predicted scenarios (BCC, MRI, IPSL, EC, CNRM models) and the SSP585 pathways.

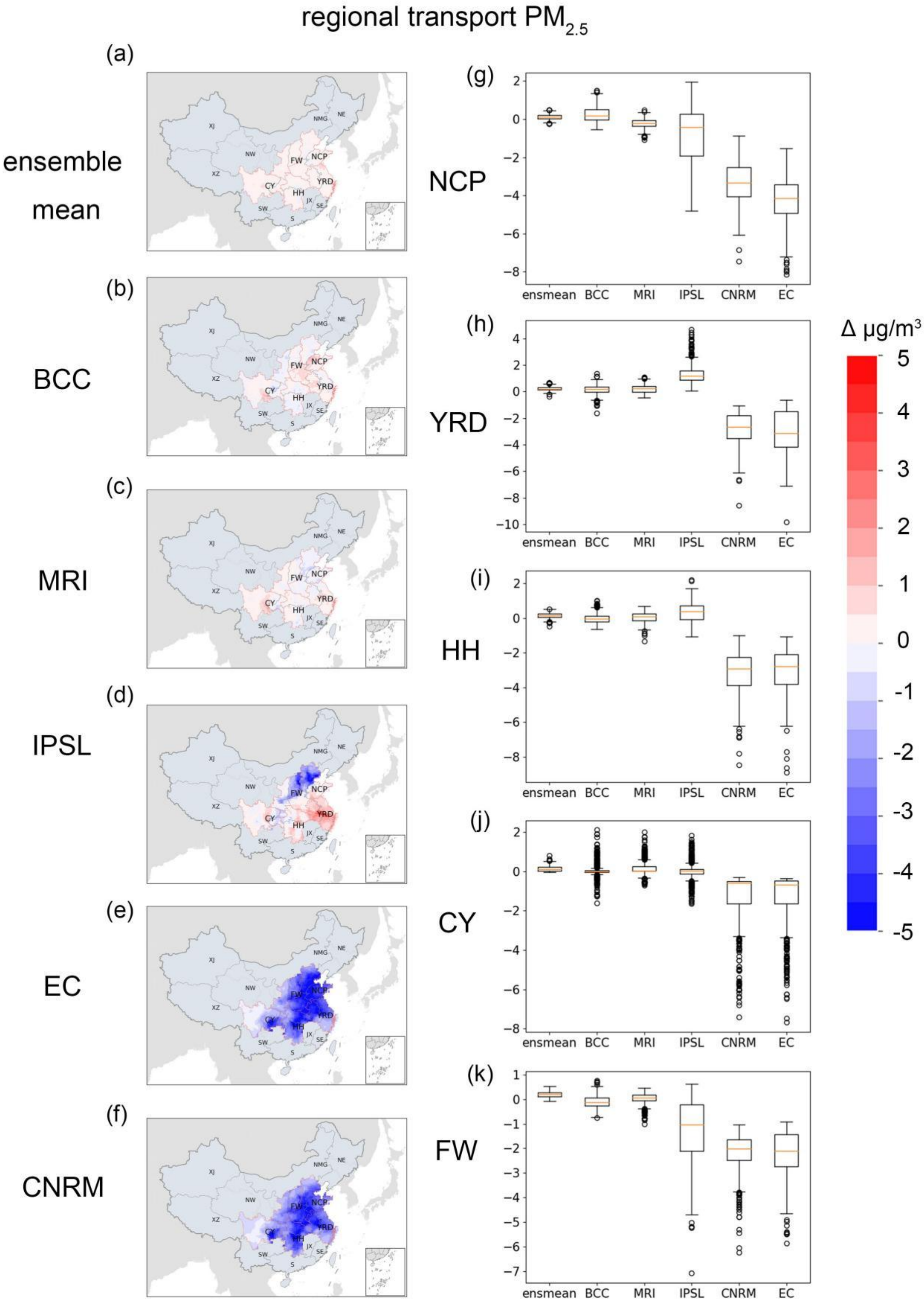

Figure S6. The left panel shows the distribution of annual average differences in simulated $PM_{2.5}$ regional transport concentrations between the SSP126 predicted scenarios (BCC, MRI, IPSL, EC, CNRM models) and the SSP585 pathways. The right panel shows the box-plot of regional transport of $PM_{2.5}$ concentrations simulated by CMIP6 multi-climate models (μg/m^3), including NCP, YRD, HH , CY and FW five target regions.

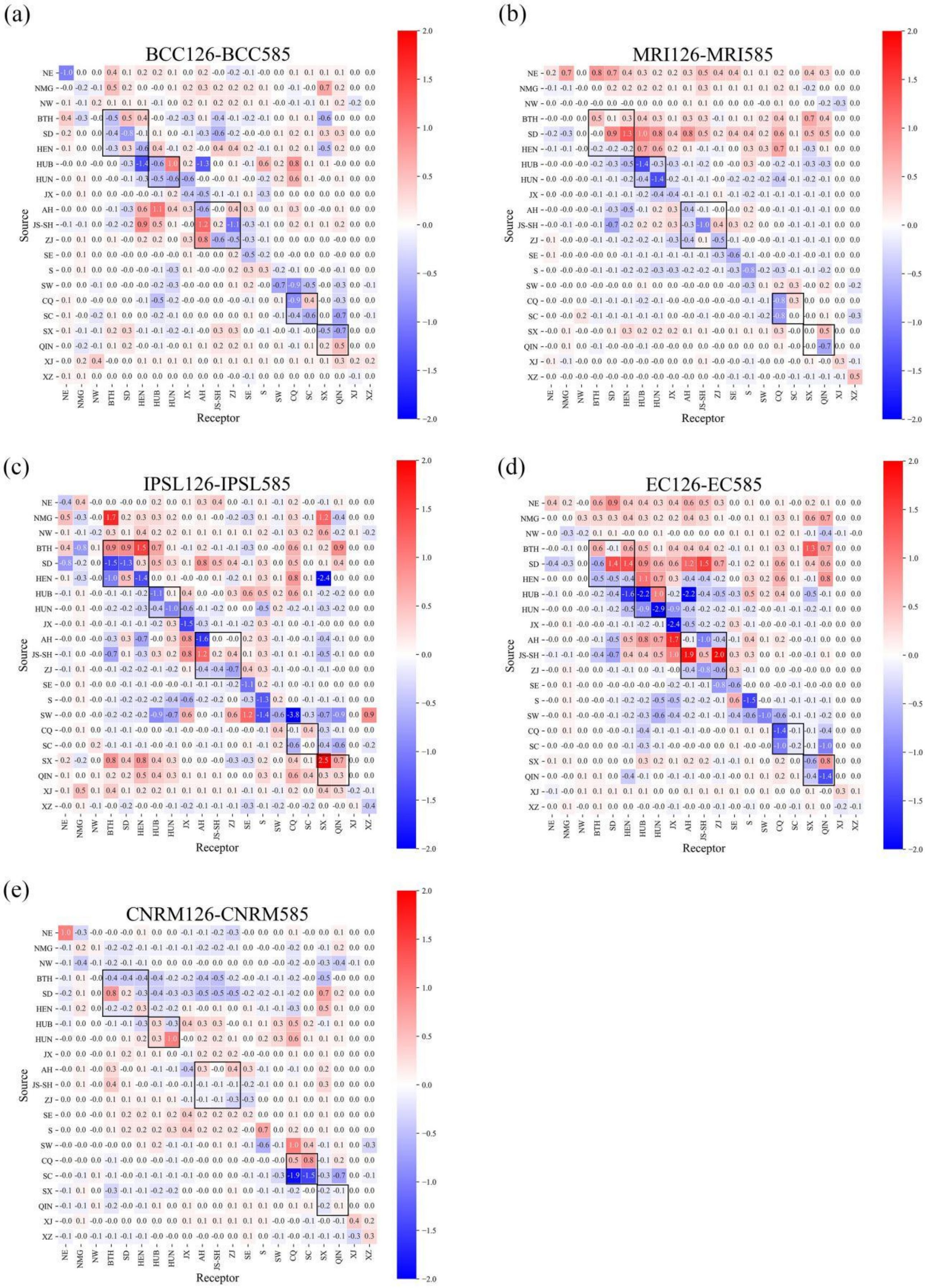

Figure S7. Regional transport matrix in different climate models (BCC, MRI, IPSL, EC, CNRM)

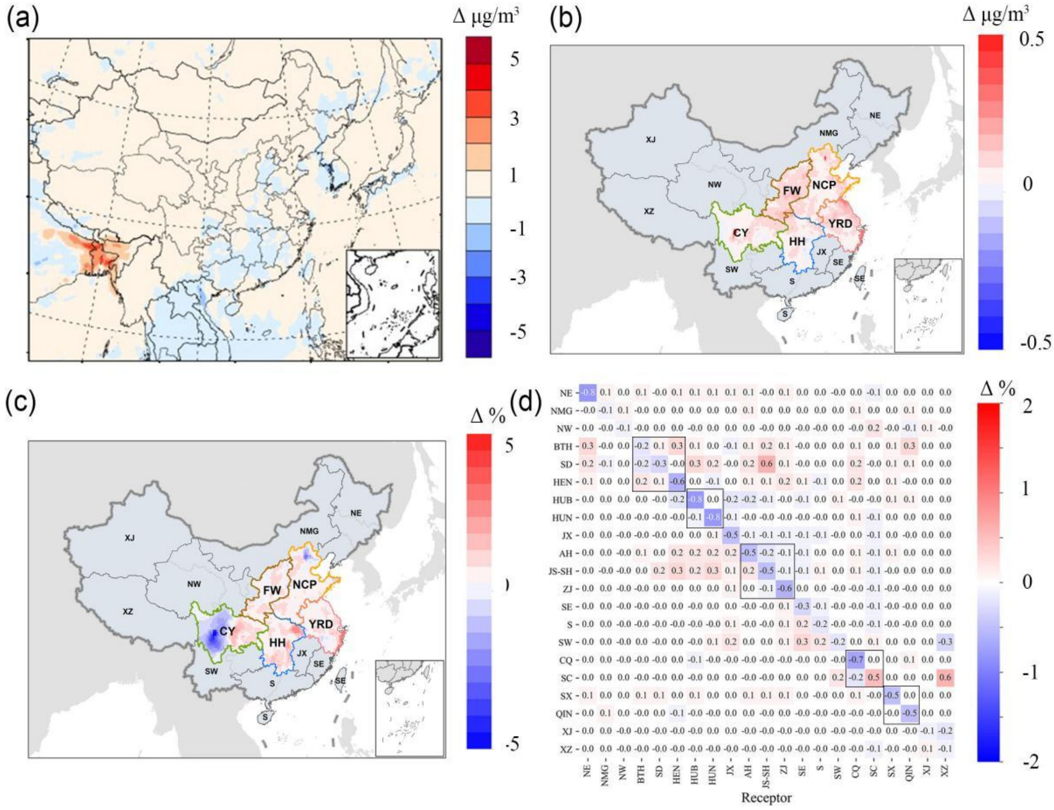

Figure S8. Similar to Figure 1, the comparison of Δmeteorology-driven $PM_{2.5}$ regional transport under CBE scenarios, (difference distribution map of regional transport between SSP126 and SSP585 scenarios)

(a) shows the changed $PM_{2.5}$ concentration (μg/m^3) , (b) shows changed absolute value (μg/m^3) and (c) shows changed relative ratio (percent), (d) shows changed regional transport (percent)

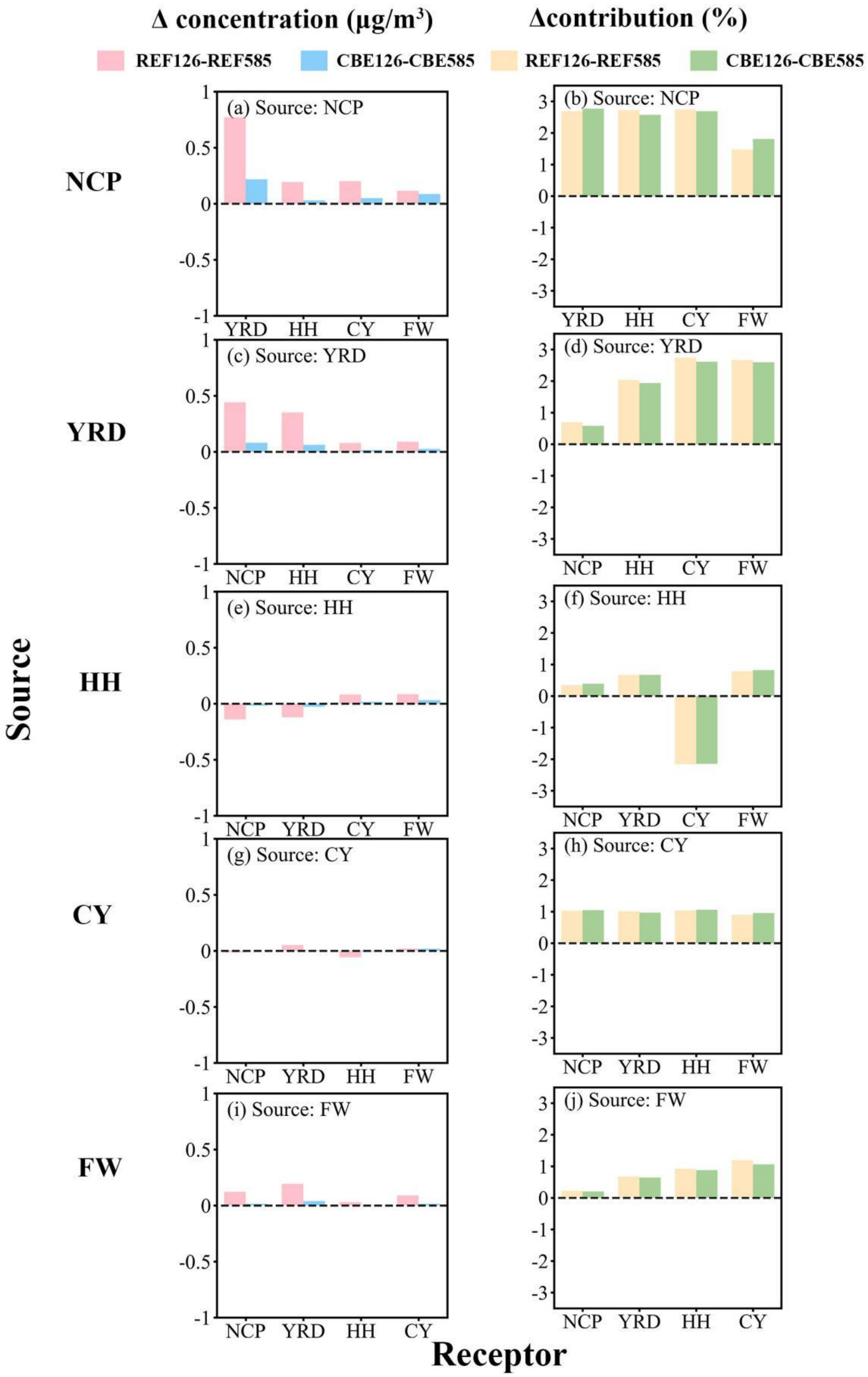

Figure S9. Similar to Figure 3, the relationship of five sources and receptors differs between SSP126 and SSP585 scenarios.. The left panel shows the change concentration of $PM_{2.5}$ regional transport and the right panel show the change contribution. The red and yellow bar show the difference between REF126 and REF 585 scenarios, blue and green bar show the difference between CBE126 and CBE 585 scenarios. Each subplot represents the effect of a single source on the other four receptors.

The future slight change of $PM_{2.5}$ concentration is associated with the higher planetary boundary layer height and increased precipitation in the 2050 global warming trend (Fig. S10), these changes are consistent with IPCC's recent reports and with high confidence (Thackeray et al., 2022), highlighting that global warming intensifies the occurrence of extreme precipitation in the future, particularly in China (Qin et al., 2021; Takahashi et al., 2020).

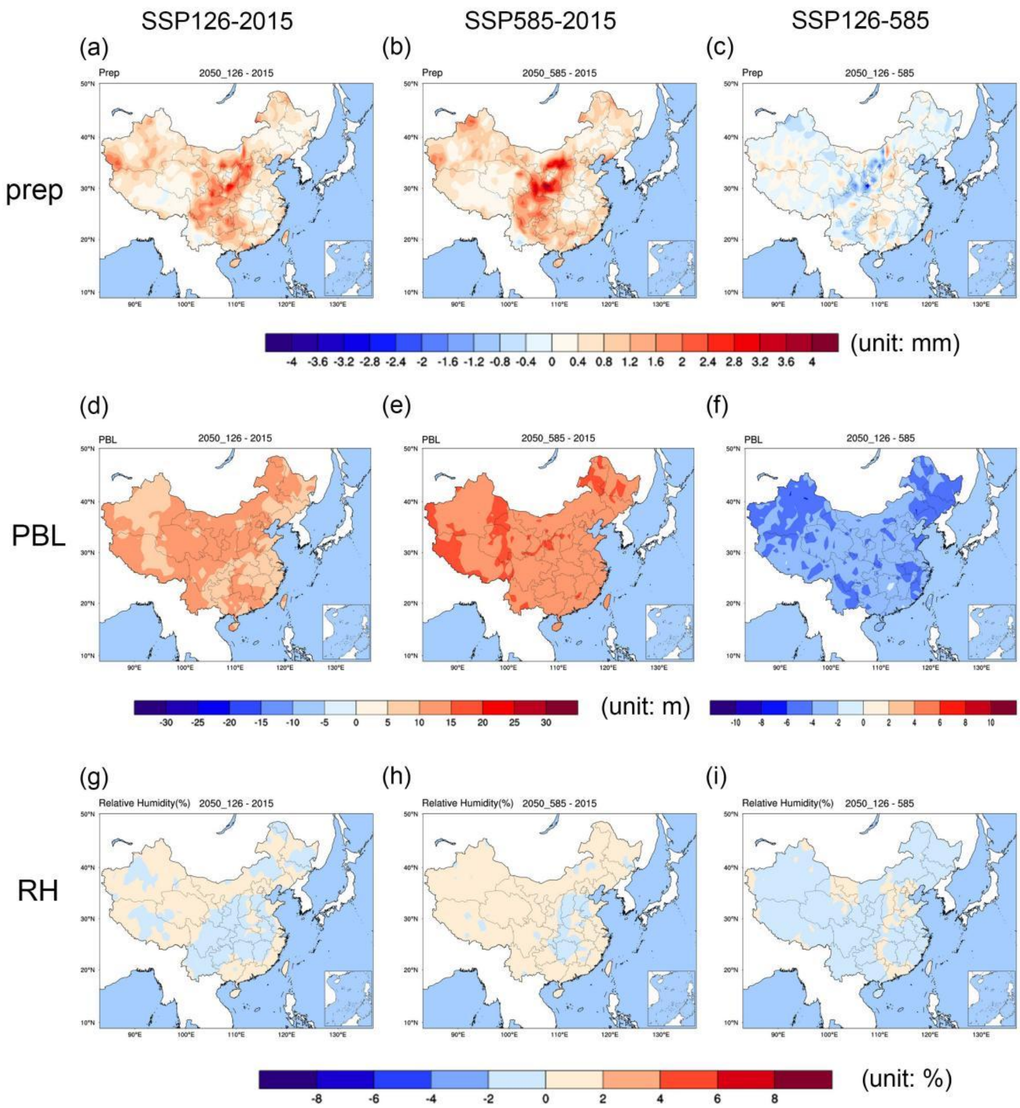

Figure S10. The difference in precipitation (mm), planetary boundary layer height (m) and relative humidity (%) between 2050 projected and 2015 baseline.

The right panel is the difference between SSP126 and 2015, the middle is the difference between SSP585 and 2015, and the right panel is the difference between SSP126 and SSP585 scenarios.

(a), (b) and (c) show the variation of precipitation (mm); (d), (e) and (f) show the variation of planetary boundary layer height (m); (g), (h) and (i) show the variation of relative humidity (%).

Reference

Qin, P., Xie, Z., Zou, J., Liu, S., and Chen, S.: Future Precipitation Extremes in China under Climate Change and Their Physical Quantification Based on a Regional Climate Model and CMIP5 Model Simulations, Adv. Atmos. Sci., 38, 460-479, 10.1007/s00376-020-0141-4, 2021.

Takahashi, H. G., Kamizawa, N., Nasuno, T., Yamada, Y., Kodama, C., Sugimoto, S., and Satoh, M.: Response of the Asian Summer Monsoon Precipitation to Global Warming in a High-Resolution Global Nonhydrostatic Model, J. Climate, 33, 8147-8164, 10.1175/JCLI-D-19-0824.1, 2020.

Thackeray, C. W., Hall, A., Norris, J., and Chen, D.: Constraining the increased frequency of global precipitation extremes under warming, Nat. Clim. Change, 12, 441-448, 10.1038/s41558-022-01329-1, 2022.

We found that the changed $PM_{2.5}$ regional transport is associated with a weakened wind field under the background of global warming (Fig. S11), which may be related to a weakening of temperature gradients between the equator and the poles, leading to a weakening of circulation. Furthermore, previous studies demonstrated that global warming results in a weakening of the global atmospheric circulation such as Hadley Cell (Kim et al., 2022; Levine and Schneider, 2011; Hu et al., 2018).

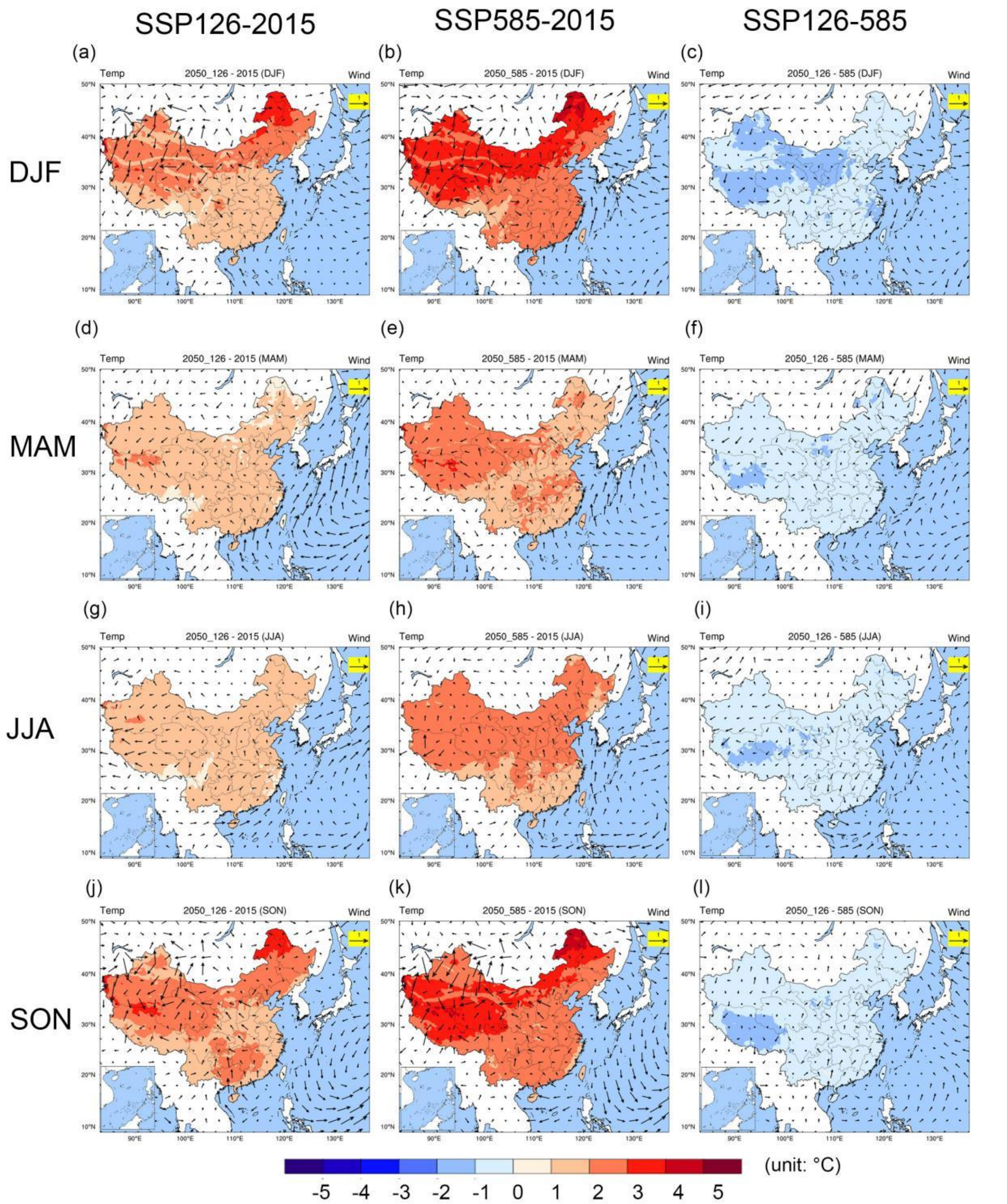

Figure S11. Similar to Figure S10, the near-surface wind field and temperature simulation in various between the 2015 baseline and 2050 projected. Temperature is represented by shading color (°C).

(a), (b) and (c) show winter (December, January, February, DJF); (d), (e) and (f) show spring (March, April, May, MAM); (g), (h) and (i) show summer(June, July, August, JJA); (j), (k) and (l) show autumn (September, October, November, SON), respectively.

Reference

Hu, Y., Huang, H., and Zhou, C.: Widening and weakening of the Hadley circulation under global warming, Science Bulletin, 63, 640-644, https://doi.org/10.1016/j.scib.2018.04.020, 2018.

Kim, D., Kim, H., Kang, S. M., Stuecker, M. F., and Merlis, T. M.: Weak Hadley cell intensity changes due to compensating effects of tropical and extratropical radiative forcing, NPJ CLIMATE AND ATMOSPHERIC SCIENCE, 5, 10.1038/s41612-022-00287-x, 2022.

Levine, X. J., and Schneider, T.: Response of the Hadley Circulation to Climate Change in an Aquaplanet GCM Coupled to a Simple Representation of Ocean Heat Transport, J. Atmos. Sci., 68, 769-783, 10.1175/2010JAS3553.1, 2011.